

Multi-objective optimization of functionally graded thick shells for thermal loading

Senthil S. Vel^{*}, Jacob L. Pelletier

Department of Mechanical Engineering, University of Maine, Orono, ME 04469, USA

Available online 17 November 2006

Abstract

Presented herein is a methodology for the multi-objective optimization of material distribution of functionally graded cylindrical shells for steady thermomechanical processes. The proposed approach focuses on isotropic metal/ceramic and metal/metal functionally graded materials, which offer great promise in high temperature and high heat flux applications. The material composition is assumed to vary only in the thickness direction. The volume fractions of the constituent material phases at a point are obtained through piecewise cubic interpolation of volume fractions defined at a finite number of evenly spaced control points. The effective material properties are estimated using the self-consistent homogenization scheme. The volume fractions at the control points, which are chosen as the design variables, are optimized using an elitist, non-dominated sorting multi-objective genetic algorithm. Candidate designs are evaluated using an exact power-series solution to the two-dimensional quasi-static heat conduction and plane strain thermoelasticity problems. The formulation, which is applicable to both thin and thick functionally graded shells, can also be used to analyze and optimize functionally graded plates in the limit that the midsurface radius of the shell approaches infinity. The proposed methodology is illustrated by optimizing the material composition profile for two model problems. In the first model problem, both the mass and the peak hoop stress of Zirconia/Titanium alloy plates and shells are simultaneously minimized for a prescribed temperature load with a constraint on the maximum temperature experienced by the metal. The goal of the second model problem is to simultaneously minimize the mass and maximize the factor of safety of Tungsten/Copper alloy functionally graded plates and shells under an applied heat flux, subject to a constraint on the factor of safety.

© 2006 Elsevier Ltd. All rights reserved.

Keywords: FGM; Inhomogeneous material; Multi-criteria optimization; Evolutionary algorithms; Genetic algorithms

1. Introduction

Functionally graded materials (FGMs) are advanced composite materials that consist of two or more material ingredients that are engineered to have a continuous spatial variation of material properties. This is achieved by gradually changing the volume fractions and/or microstructure of the constituent materials during fabrication. The constituent material phases for FGMs are chosen based on functional performance requirements. For example, metal/ceramic FGMs are primarily used in high temperature

applications. Typically, ceramic-rich material would be used in the high temperature regions and metal-rich material would be placed at locations where mechanical properties, such as toughness, need to be high. FGMs permit tailoring of material composition so as to derive maximum benefits from their inhomogeneity and they offer great promise in applications where the operating conditions are severe, including spacecraft heat shields, coatings on gas turbine blades, plasma facings for fusion reactors, etc. [1]. In the case of the future International Thermonuclear Experimental Reactor (ITER), the plasma divertor must survive high heat flux loads, and in addition, must efficiently transfer heat energy to an active cooling mechanism [2,3]. Numerous designs have been developed for

^{*} Corresponding author. Tel.: +1 207 581 2777.
E-mail address: senthil.vel@maine.edu (S.S. Vel).

potential use in ITER, most of which involve Tungsten as the plasma facing material and Copper alloy as the actively cooled component. However, if the divertor component is fabricated by simply bonding a Tungsten plasma facing to a Copper alloy base, the abrupt transition in material properties across the interface between these distinct materials can lead to severe thermal stresses and premature failure. This can be alleviated by using a graded material architecture. Several analytical solutions and numerical formulations have been developed for the thermoelastic analysis of FGMs (e.g. see [4–8]).

It is important to note that the performance of a FGM is not just a function of the properties of its material constituents alone, but is directly related to the ability of the designer to utilize the materials in the most optimal fashion. Thus, the optimization of material distribution is a crucial step in the design of functionally graded components. To date, research pertaining to the optimization of FGMs is comprised almost entirely of single-objective studies [9–18]. However, the design of practical FGMs often require the maximization or minimization of multiple, often conflicting, objectives. In general, a multi-objective optimization algorithm will yield a set of optimal solutions, instead of a single optimal solution. The reason for the optimality of many solutions is that no one solution can be considered better than any other with respect to all the objective functions. These optimal solutions are known as Pareto-optimal solutions [19,20]. The only known work to date which considers the multi-objective optimization of FGMs was performed by Huang et al. [21]. They performed a bi-objective optimization design of functionally graded flywheels with general one-dimensional grading profiles and radially varying thicknesses using a weighted Tchebycheff method. There is a lack of research on the multi-objective optimization of functionally graded materials for thermomechanical processes.

In this article, a methodology for the multi-objective optimization of material distribution of simply supported functionally graded plates and shells is presented. This is accomplished by representing the volume fraction variation of an isotropic FGM shell using piecewise cubic Hermite polynomials. The volume fraction at a point is obtained through range-restricted interpolation of volume fractions at a finite number of control points that are evenly spaced in the thickness direction [22]. The volume fractions at the control points are chosen as the design variables since they can be varied to obtain different continuous volume fraction profiles. A power-series analysis procedure that was originally developed for anisotropic shells [23] is adapted to obtain an exact solution to the heat-conduction and plane strain thermoelasticity problems for the isotropic functionally graded thick shells and plates considered here. The volume fraction profile is optimized using an elitist non-dominated sorting genetic algorithm [24,25]. The proposed methodology is demonstrated using two model problems. In the first

model problem, Zirconia/Titanium functionally graded plates and shells that are exposed to a high temperature load on the top surface are considered. Optimal material composition profiles are obtained by simultaneously minimizing both the mass and the peak hoop stress subject to a constraint on the maximum temperature experienced by the metal. In the second model problem, Tungsten/Copper functionally graded plates and shells that are exposed to a high heat flux on the top surface are optimized. Thermal softening effects are taken into account by considering the temperature dependent yield strengths of Tungsten and Copper. The volume fraction profile is tailored by simultaneously minimizing the mass and maximizing the factor of safety subject to a constraint on the factor of safety.

The paper is organized as follows. In Section 2 the range-restricted piecewise cubic interpolation of the volume fraction and the estimation of effective material properties are discussed. The formulation and power-series analytical solution of the heat conduction and thermoelasticity problems are described in Section 3. Details about the multi-objective optimization algorithm are given in Section 4. In Section 5, the proposed method is used to analyze and optimize the material distribution for two model problems. The results demonstrate that the proposed methodology provides a framework for designing functionally graded plates and shells for multiple, often conflicting, design objectives.

2. Representation of material composition profile

The geometry of a functionally graded cylindrical shell using a global, cylindrical coordinate system, with coordinates r , θ and x denoting the radial, circumferential and axial coordinate directions, respectively, is depicted in Fig. 1. The shell is assumed to be of infinite extent in the axial direction. In this coordinate system, the functionally graded shell occupies the region $[R_i, R_o] \times [0, \Theta] \times (-\infty, \infty)$, where R_i , R_o and Θ denote the inner radius, the outer radius and the angular span, respectively. It is assumed that the material properties of the shell vary only in the radial direction.

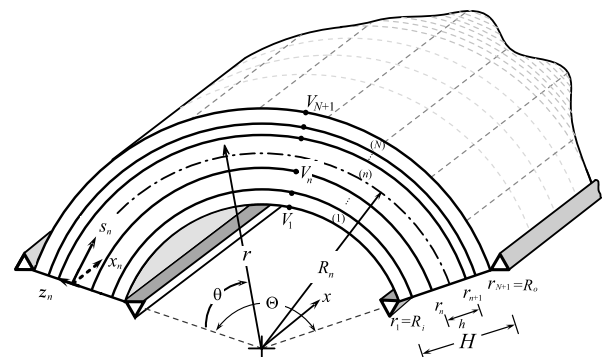


Fig. 1. Graphical depiction of a multilayer FGM cylindrical shell of infinite axial extent.

2.1. Volume fraction distribution

The optimization of the material distribution of a two-phase functionally graded material is equivalent to the optimization of the volume fraction distribution $V(r)$ of one of its constituent phases. A direct pointwise optimization of the volume fraction at every radial location is computationally intractable. Therefore, the present formulation utilizes a finite number of control points in the radial direction to reduce the number of design variables. The volume fraction at an arbitrary radial location is obtained via piecewise cubic interpolation from the volume fractions at the control points. Thus, the volume fraction distribution in the thickness direction of the shell can be tailored using the volume fraction values at the control points.

A total of $N + 1$ equally spaced control points in the radial direction at locations $r_n = R_i + (R_o - R_i)(n - 1)/N$ is utilized, where $n = 1, \dots, N + 1$. The volume fraction at the control point located at r_n is denoted by V_n . In the present formulation, the volume fractions V_1, \dots, V_{N+1} at the control points are treated as the design variables. The physical constraints of the problem require that the interpolated volume fraction be strictly in the range of zero to one at all points within the domain, i.e., $0 \leq V(r) \leq 1$. In order to obtain smooth material composition profiles, a range-restricted piecewise cubic interpolation for the volume fraction [22] is employed. This method, which is based on sufficiency conditions for univariate piecewise cubic interpolation to preserve positivity [26], performs range-restricted interpolation while preserving \mathcal{C}^1 continuity. The restriction of the interpolant to remain between desired bounding values is achieved by setting upper and lower limits on the slope of the interpolated volume fraction distribution at the control points.

The volume fraction distribution $V(r)$ in the interval $r \in [r_n, r_{n+1}]$ is interpolated as follows:

$$V(r) = V_n H_1(r) + S_n H_2(r) + V_{n+1} H_3(r) + S_{n+1} H_4(r), \quad (1)$$

where V_n and S_n denote the volume fraction and slope of the volume fraction distribution, respectively, at the control points located at r_n . The functions $H_k(r)$ are the Hermite basis functions (e.g. see [27]),

$$\begin{aligned} H_1(r) &= \frac{2}{h^3} \left(r - r_n + \frac{h}{2} \right) (r - r_{n+1})^2, \\ H_2(r) &= \frac{1}{h^2} (r - r_n) (r - r_{n+1})^2, \\ H_3(r) &= -\frac{2}{h^3} (r - r_n)^2 \left(r - r_{n+1} - \frac{h}{2} \right), \\ H_4(r) &= \frac{1}{h^2} (r - r_n)^2 (r - r_{n+1}), \end{aligned} \quad (2)$$

where $h = r_{n+1} - r_n = (R_o - R_i)/N$. In order to completely specify the interpolated volume fraction distribution $V(r)$, it is apparent from (1) that the slopes S_n at the control points must be supplied in some manner. The volume fraction values V_n at the control points are chosen as the design

variables in the present formulation. Although the slopes S_n may also be considered as design variables, it is advantageous to estimate them based on the neighboring control point values, since this will result in a smaller set of design variables and a more efficient optimization algorithm. In the present work, the slopes are estimated based on a 3-point centered finite difference formula,

$$S_n = (V_{n+1} - V_{n-1})/2h \quad \text{for } n = 2, 3, \dots, N. \quad (3)$$

The slopes at the top and bottom surfaces of the shell are evaluated based on one sided finite difference formulae,

$$\begin{aligned} S_1 &= (-3V_1 + 4V_2 - V_3)/2h, \\ S_{N+1} &= (3V_{N+1} - 4V_N + V_{N-1})/2h. \end{aligned} \quad (4)$$

With the slopes of the volume fraction distribution estimated at the control points, they must be checked to make sure that they are within certain upper and lower bounds to achieve proper range restriction of the volume fraction distribution. The appropriate bounds are given by Brodlić et al. [22]. If the estimated slopes lie outside these bounds, the estimated values are simply projected on to the valid range. For the interior control points the valid range of the slopes are as follows:

$$\begin{aligned} \text{Max}\{-3(1 - V_n)/h, -3V_n/h\} &\leq S_n \\ &\leq \text{Min}\{3(1 - V_n)/h, 3V_n/h\}, \end{aligned} \quad (5)$$

for $n = 2, 3, \dots, N$. Corresponding one-sided conditions for the first and last control points are,

$$\begin{aligned} -3V_1/h &\leq S_1 \leq 3(1 - V_1)/h, \\ -3(1 - V_{N+1})/h &\leq S_{N+1} \leq 3V_{N+1}/h. \end{aligned} \quad (6)$$

If the slope at a control point, estimated using (3) or (4), happens to lie outside the valid upper and lower bounds stated in (5) or (6), it is corrected by setting it equal to the violated bound. This ensures that the interpolated volume fraction distribution satisfies the physical constraints, $0 \leq V(r) \leq 1$, at every point within the domain provided that the design variables V_n are constrained to lie in the range $[0, 1]$.

2.2. Effective moduli of two-phase composite materials

Consider a functionally graded composite material that is fabricated by mixing two distinct material phases, for example, a metal and a ceramic. Often, precise information about the size, shape and distribution of the particles may not be available and the effective moduli of the graded composite must be evaluated based only on the volume fraction distributions and the approximate shape of the dispersed phase. Several micromechanics models have been developed over the years to infer the effective properties of macroscopically homogeneous composite materials. In the present work, the effective material properties are estimated using the self-consistent method [28].

The self-consistent method assumes that each reinforcement inclusion is embedded in a continuum material whose

effective properties are those of the composite. It is assumed that K_1 , μ_1 , κ_1 and α_1 denote the bulk modulus, the shear modulus, the thermal conductivity and the thermal expansion coefficient, respectively, of the first material phase, and V denotes its volume fraction. The corresponding material properties of the second material phase are denoted by K_2 , μ_2 , κ_2 , and α_2 . For two-phase functionally graded materials considered here, the volume fraction of the second material phase is $1 - V$. The locally effective bulk, K , and shear moduli, μ , obtained using the self-consistent method are

$$\begin{aligned} \delta/K &= V/(K - K_2) + (1 - V)/(K - K_1), \\ \eta/\mu &= V/(\mu - \mu_2) + (1 - V)/(\mu - \mu_1), \end{aligned} \quad (7)$$

where $\delta = 3 - 5\eta = K/(K + 4\mu/3)$. These are implicit expressions for the unknowns K and μ . The first equation in (7) can be solved to determine K in terms of μ ,

$$K = 1/(V/(K_1 + 4\mu/3) + (1 - V)/(K_2 + 4\mu/3)) - 4\mu/3, \quad (8)$$

and μ is obtained by solving the following quartic equation:

$$\begin{aligned} [VK_1/(K_1 + 4\mu/3) + (1 - V)K_2/(K_2 + 4\mu/3)] \\ + 5[V\mu_2/(\mu - \mu_2) + (1 - V)\mu_1/(\mu - \mu_1)] + 2 = 0. \end{aligned} \quad (9)$$

The self-consistent estimate of the thermal conductivity coefficient, κ , is in the implicit form [29]

$$V(\kappa_1 - \kappa)/(\kappa_1 + 2\kappa) + (1 - V)(\kappa_2 - \kappa)/(\kappa_2 + 2\kappa) = 0, \quad (10)$$

and the coefficient of thermal expansion, α , is determined from the correspondence relation [30]

$$(\alpha - \alpha_1)/(\alpha_2 - \alpha_1) = (1/K - 1/K_1)/(1/K_2 - 1/K_1). \quad (11)$$

3. Analysis of the heat conduction and thermomechanical problems

The functionally graded shell is partitioned into N functionally graded layers by introducing $N - 1$ hypothetical interfaces in the radial direction. These interfaces are chosen to coincide with the location of the control points, r_n , for $n = 2, \dots, N$. Each layer is assumed to have a smooth variation of material properties in the radial direction due to the range-restricted cubic interpolation of the volume fraction. A particular layer of the shell, denoted by the superscript n , extends from r_n to r_{n+1} in the radial direction. In order to provide a more general shell solution that is also applicable to flat plates, a layer-wise, local circumferential coordinate system with coordinate directions, s_n , x_n , and z_n having the origin at the left edge ($\theta = 0$) of n th layer's midsurface is introduced as shown in Fig. 1. The local circumferential coordinate system is related to the global cylindrical coordinate system through the transformations

$$s_n = R_n\theta, \quad z_n = r - R_n, \quad x_n = x, \quad (12)$$

where s_n and z_n are the local arc length and local thickness coordinate, respectively, with respect to the midsurface of the n th lamina. The midsurface radius R_n and midsurface circumferential length S_n of each layer are defined as

$$R_n = \frac{1}{2}(r_n + r_{n+1}), \quad S_n = R_n\Theta. \quad (13)$$

In the local circumferential coordinate system, the n th layer occupies a region in \mathbb{R}^3 space denoted by $[-h/2, h/2] \times [0, S_n] \times (-\infty, \infty)$. Henceforth, the subscript n is omitted for simplicity of notation with the understanding that all material constants, geometric parameters and solution variables are for the n th layer is dropped unless the layer number is explicitly denoted by a subscript. Since the applied loads and material properties are independent of x and the body is of infinite extent in the x -direction, it is postulated that the change in temperature from the stress-free reference configuration, T , and displacement components, u_r and u_s , are functions of z and s only. The axial component of the displacement, u_x , is assumed to be zero. Thus, the functionally graded shell is assumed to be in a state of plane strain.

Fourier's law of heat conduction, which relates the heat flux to the temperature gradient, in the local circumferential coordinate system is

$$q_s = -\kappa \frac{R}{R+z} \frac{\partial T}{\partial s}, \quad q_r = -\kappa \frac{\partial T}{\partial z}, \quad (14)$$

where κ is the thermal conductivity. The thermomechanical constitutive equations, which relate the stresses to the deformation and change in temperature, are

$$\begin{aligned} \sigma_{ss} &= (\lambda + 2\mu) \left(\frac{R}{R+z} \frac{\partial u_s}{\partial s} + \frac{u_r}{R+z} \right) + \lambda \frac{\partial u_r}{\partial z} - \beta T, \\ \sigma_{xx} &= \lambda \left(\frac{R}{R+z} \frac{\partial u_s}{\partial s} + \frac{u_r}{R+z} + \frac{\partial u_r}{\partial z} \right) - \beta T, \\ \sigma_{rr} &= (\lambda + 2\mu) \frac{\partial u_r}{\partial z} + \lambda \left(\frac{R}{R+z} \frac{\partial u_s}{\partial s} + \frac{u_r}{R+z} \right) - \beta T, \\ \sigma_{rs} &= \mu \left(\frac{R}{R+z} \frac{\partial u_r}{\partial s} + \frac{\partial u_s}{\partial z} - \frac{u_s}{R+z} \right), \end{aligned} \quad (15)$$

where λ and μ are Lamé constants and β is the stress-temperature moduli. It should be noted that the Lamé constant, λ , is related to the bulk and shear moduli by $\lambda = K - 2\mu/3$ and the stress-temperature modulus, β , is determined from the bulk modulus and thermal expansion coefficient using the relation $\beta = 3K\alpha$. Since the shell is graded in the radial direction, the material properties κ , λ , μ , and β are functions of the radial coordinate z .

Assuming that internal heat sources and body forces are absent, the three-dimensional steady-state heat conduction equation, expressed in terms of the local coordinates, is

$$\frac{\partial q_r}{\partial z} + \frac{R}{R+z} \frac{\partial q_s}{\partial s} + \frac{q_r}{R+z} = 0, \quad (16)$$

where q_r and q_s are the components of the heat flux vector. The corresponding mechanical equilibrium equations, are

$$\begin{aligned} \frac{\partial \sigma_{rr}}{\partial z} + \frac{R}{R+z} \frac{\partial \sigma_{rs}}{\partial s} + \frac{\sigma_{rr} - \sigma_{ss}}{R+z} &= 0, \\ \frac{\partial \sigma_{rs}}{\partial z} + \frac{R}{R+z} \frac{\partial \sigma_{ss}}{\partial s} + \frac{2\sigma_{sr}}{R+z} &= 0, \end{aligned} \tag{17}$$

where σ_{rr} , σ_{ss} , and σ_{rs} are the components of the Cauchy stress tensor in a circumferential coordinate system.

Since the shell is viewed as a three-dimensional body, it is necessary to prescribe either a displacement or traction component in each coordinate direction at every point on the boundary. It is assumed that the shell is simply supported and maintained at the constant ambient reference temperature at the edges and the following mixed boundary conditions are prescribed

$$u_r = 0, \quad \sigma_{ss} = 0, \quad T = 0 \text{ at } s = 0, S. \tag{18}$$

Additional thermal and mechanical boundary conditions are imposed on the inner and outer surfaces of the shell as follows:

$$\begin{aligned} \vartheta^- T + \xi^- q_r &= \chi^- \sin \frac{k\pi s_1}{S_1}, \quad \sigma_{rr} = \sigma_{sr} = 0 \text{ at } z_1 = -h/2, \\ \vartheta^+ T + \xi^+ q_r &= \chi^+ \sin \frac{k\pi s_N}{S_N}, \quad \sigma_{rr} = \sigma_{sr} = 0 \text{ at } z_N = h/2, \end{aligned} \tag{19}$$

where χ^- and χ^+ denote the amplitude of the thermal loads which are sinusoidal in the circumferential direction and k is a positive integer that specifies the harmonic of the sinusoidal load. Various thermal boundary conditions, corresponding to either prescribed temperatures or heat fluxes or exposure to ambient temperature through boundary convection, are specified by appropriately choosing the constants ϑ^- , ξ^- , ϑ^+ , and ξ^+ . The functionally graded layers are assumed to be in ideal thermal contact and perfectly bonded together and the following thermal and mechanical continuity conditions are assumed at the interfaces $r = r_n$ for $n = 1, \dots, N - 1$ (e.g. see [31,32])

$$[[T]] = 0, \quad [[q_r]] = 0, \quad [[u_r]] = [[u_s]] = 0, \quad [[\sigma_{rr}]] = [[\sigma_{sr}]] = 0, \tag{20}$$

where $[[g]]$ denotes the jump in the value of g across the interface.

It is assumed that the material properties of each layer of the functionally graded shell are analytic functions of the radial coordinate z , and, thus, can be represented by a Taylor series expansion about its midsurface as

$$[\kappa, \lambda, \mu, \beta] = \sum_{b=0}^{\infty} [\kappa_b, \lambda_b, \mu_b, \beta_b] z^b. \tag{21}$$

3.1. Temperature and heat flux

A semi-inverse solution to the heat conduction problem is sought by assuming a power series form for the temperature field

$$T = \left(\sum_{b=0}^{\infty} \eta_b z^b \right) \sin ps, \tag{22}$$

where $p = k\pi/S$. The assumed form of the temperature field identically satisfies the homogeneous boundary conditions (18) for the temperature at the edges. Substitution for T from (22) into (14) yields the components of the heat flux vector. Substitution of the heat flux vector into (16) and equating like powers of z , results in the following recurrence relation

$$\begin{aligned} \sum_{b=0}^a \{ &(a-b+1)(a-b+2)\kappa_b \eta_{a-b+2} \\ &+ (b+1)(a-b+1)\kappa_{b+1} \eta_{a-b+1} \\ &+ \sum_c^{a-b} [(a-b-c+1)\phi_b \kappa_c \eta_{a-b-c+1} - \psi_b p^2 \kappa_c \eta_{a-b-c}] \} = 0, \end{aligned} \tag{23}$$

which has to hold true for every $a = 0, 1, 2, \dots$. Here $\phi_b = (-1)^b/R^{b+1}$ and $\psi_b = (b+1)(-1)^b/R^b$. The recurrence relation (23) is evaluated successively for $a = 0, 1, \dots$ to obtain the coefficients η_{a+2} in terms of two constants η_0 and η_1 . The power series coefficients η_b are then inserted into (22) to obtain the change in temperature T and heat flux q through (14), in terms of two constants, namely η_0 and η_1 , for each layer. For an N -layer shell, the power series solution procedure results in $2N$ constants. The constants are determined by satisfying the thermal boundary conditions (19) on the top and bottom surfaces of the shell and the thermal continuity conditions (20) at each of the $N - 1$ interfaces. The resulting system of $2N$ linear algebraic equations for the $2N$ unknowns is readily solved to obtain η_0 and η_1 for each layer. The series coefficients η_b , thus obtained, are reinserted into (22) to yield the temperature field for each layer. The temperature and heat flux for a flat plate are obtained by setting $R \rightarrow \infty$ in the series coefficients ϕ_b and ψ_b .

3.2. Displacements and stresses

With the temperature field established, a semi-inverse solution for the displacement field is sought by assuming that

$$u_s = \left(\sum_{b=0}^{\infty} U_b z^b \right) \cos ps, \quad u_r = \left(\sum_{b=0}^{\infty} W_b z^b \right) \sin ps. \tag{24}$$

The simply supported boundary conditions at the edges of a layer are identically satisfied by the assumed displacement field. Substitution of the assumed displacement field (24) and the Taylor series expansions of the material properties (21) into the constitutive Eq. (15) and the equilibrium Eq. (17), yield the following recurrence relations

$$\sum_{b=0}^a \{ (a-b+1)(a-b+2)(\lambda_b + 2\mu_b)W_{a-b+2} + (b+1)(a-b+1)(\lambda_{b+1} + 2\mu_{b+1})W_{a-b+1} - (a-b+1)\beta_b \eta_{a-b+1} - (b+1)\beta_{b+1} \eta_{a-b} + \sum_{c=0}^{a-b} [\psi_b [(-\frac{1}{R^2}(\lambda_c + 2\mu_c) - p^2 \mu_c)W_{a-b-c} + \frac{p}{R}(\lambda_c + 3\mu_c)U_{a-b-c}] + \phi_b [(c+1)\lambda_{c+1}W_{a-b-c} + (a-b-c+1)(\lambda_c + 2\mu_c)W_{a-b-c+1}] + \zeta_b [-p(c+1)\lambda_{c+1}U_{a-b-c} - p(a-b-c+1)(\lambda_c + \mu_c)U_{a-b-c+1}]] \} = 0, \tag{25}$$

$$\sum_{b=0}^a \{ (a-b+1)(a-b+2)\mu_b U_{a-b+2} + (b+1)(a-b+1)\mu_{b+1} U_{a-b+1} + \sum_{c=0}^{a-b} [\psi_b [\frac{p}{R}(\lambda_c + 3\mu_c)W_{a-b-c} - p^2 R^2(\lambda_c + 2\mu_c + \frac{1}{p^2 R^2} \mu_c)U_{a-b-c}] + \zeta_b [-p\beta^{(c)} \eta_{a-b-c} + p(c+1)\mu_{c+1}W_{a-b-c} + p(a-b-c+1)(\lambda_c + \mu_c)W_{a-b-c+1}] + \phi_b [-(c+1)\mu_{c+1}U_{a-b-c} + (a-b-c+1)\mu_c U_{a-b-c+1}]] \} = 0, \tag{26}$$

which have to hold true for every $a = 0, 1, 2, \dots$. Here $\zeta_b = (-1)^b/R^b$. The recurrence relations (25) and (26) are evaluated successively for $a = 0, 1, \dots$ to obtain two simultaneous equations, which are solved to obtain U_{a+2} and W_{a+2} in terms of four unknown constants U_0, U_1, W_0 and W_1 . The power series coefficients U_b and W_b are inserted into (24) to obtain the components of the displacement field u_s and u_r in terms of the four constants for each layer. For an N -layer shell, the power series solution procedure results in $4N$ constants. The constants are determined by satisfying the traction boundary conditions (19) on the top and bottom surfaces of the shell and the mechanical continuity conditions (20) at each of the $N - 1$ interfaces. The resulting system of $4N$ linear algebraic equations for the $4N$ unknowns is readily solved to obtain $U_0, U_1, W_0,$ and W_1 for each layer. The solution for a flat plate is obtained by setting the midsurface radius $R \rightarrow \infty$ in the recurrence relations (25) and (26) for all layers.

4. Optimization using a genetic algorithm

4.1. Formulation of the multi-objective optimization problem

In the present formulation, optimization of material distribution is achieved by tailoring the volume fractions values at the control points. A constrained optimization problem is written in the following form:

$$\begin{aligned} &\text{Find } \mathbf{V}, \\ &\text{Maximize } f_i(\mathbf{V}), \quad i = 1, 2, \dots, A, \\ &\text{Subject to } g_j(\mathbf{V}) \leq 0, \quad j = 1, 2, \dots, B, \\ &\quad 0 \leq V_n \leq 1, \quad n = 1, 2, \dots, N + 1, \end{aligned} \tag{27}$$

where $\mathbf{V} = [V_1, V_2, \dots, V_{N+1}]$ is the vector of volume fractions at the control points, $f_i(\mathbf{V})$ is the i th objective function to be minimized and $g_j(\mathbf{V})$ is the j th inequality constraint. In the above problem, there are $N + 1$ optimization parameters. It should be noted that if it is desired

to minimize one or more objective function, the duality principle [20] states that a minimization problem can be converted to a maximization problem by multiplying the corresponding objective function values by -1 . Specific forms of the objective functions and inequality constraints are considered in Section 5.

4.2. The genetic algorithm

The Pareto-optimal designs are obtained using a discrete-coded version of the non-dominated sorting genetic algorithm (NSGA-II) [24,25]. A genetic algorithm works with a population of M individuals. Each individual consists of a single chromosome which, for the present volume fraction optimization problem, is chosen to contain integer-coded values of the volume fractions at the control points

$$\mathbf{X} = [I_1 I_2 \dots I_n \dots I_{N+1}], \tag{28}$$

where I_n is an integer value between 0 and \mathcal{J}_{\max} . The value of the volume fraction at the n th control point can be inferred from the integer I_n using the relation $V_n = I_n/\mathcal{J}_{\max}$. Finer resolution of the volume fractions at the control points can be obtained by choosing a larger value for \mathcal{J}_{\max} . In order to compute the objective functions and constraints for an individual \mathbf{X} , first the radial volume fraction profile is constructed from the volume fraction values at the control points. Next, a thermomechanical analysis for a given set of loads will yield the temperature, heat flux, displacement and stress fields. These values are then utilized to create and assign the values of the objective functions, $f_i(\mathbf{X})$, and constraint violations, $g_j(\mathbf{X})$, corresponding to the individual \mathbf{X} . Thus the objective functions and constraint violations of the entire population can be obtained.

The NSGA-II algorithm has been modified to include an archive of the historically non-dominated individuals, H_t . A schematic of the process that is used to update the parent population, P_t , offspring population, Q_t , and historical archive of non-dominated solutions, H_t , from generation

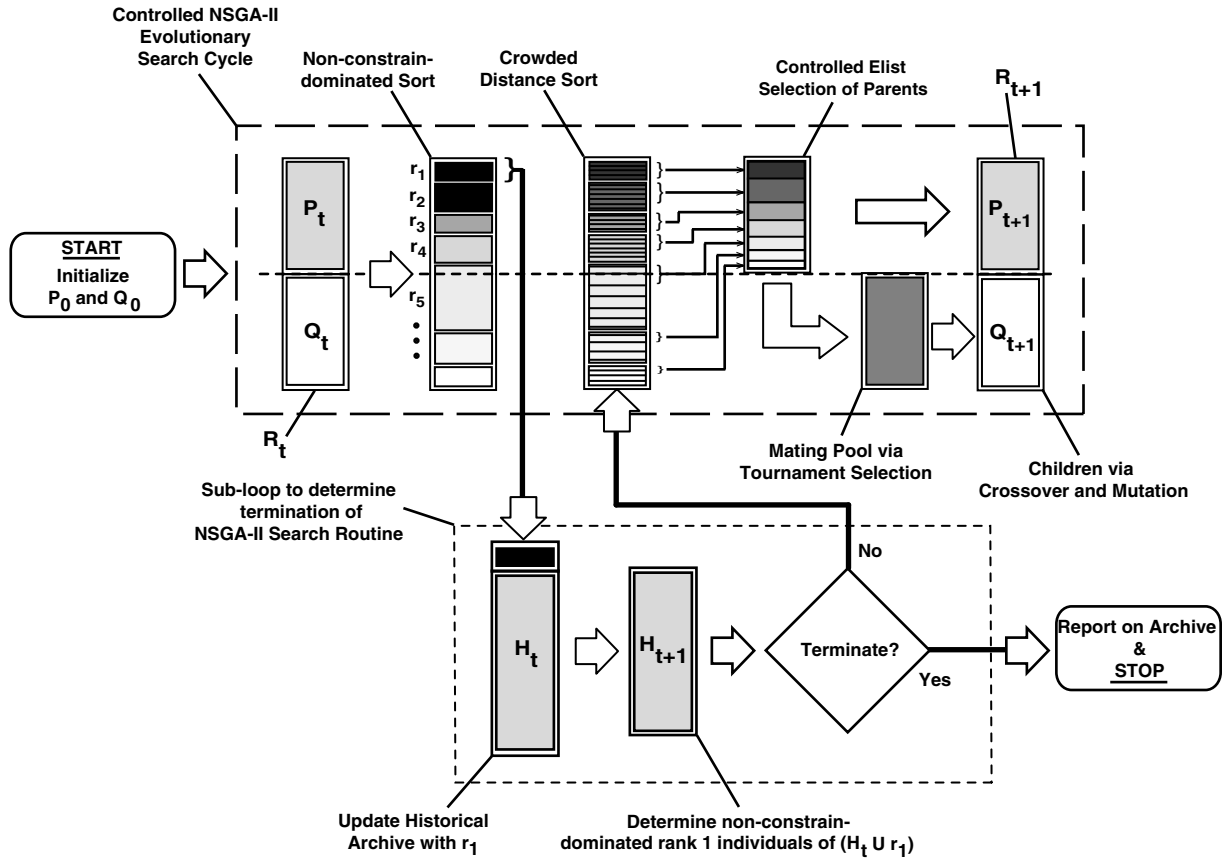


Fig. 2. Schematic of the controlled elitist non-dominated sorted multi-objective genetic algorithm with historical archive.

t to $t + 1$ is shown in Fig. 2. Details about each step of the multi-objective genetic algorithm are given below in Sections 4.2.1–4.2.5. The genetic algorithm begins at generation $t = 0$, with a random set of individuals for P_0 and Q_0 . The process of updating the individuals using NSGA-II from generation t to $t + 1$ is as follows. The parent population, P_t , and offspring population, Q_t , each consisting of M individuals, are combined to form a population, R_t . The objective functions and constraint violations of each individual in R_t are computed and they are non-dominated sorted and ranked. The archive of non-dominated solutions H_t is updated to include the better ranked individuals. Next, a crowded distance sort of the individuals is performed within each rank of R_t and a controlled elitist selection process is used to form an updated parent population, P_{t+1} . Subsequently, an intermediate mating pool is obtained from the parent population, P_{t+1} , using a crowded tournament selection operation and the offspring population, Q_{t+1} , is generated by crossover and mutation. The process is iterated over several generations and the algorithm is terminated when it fails to yield significant improvements to the non-dominated historical archive H_t . Upon termination, the set of non-dominated individuals H_t are the numerically obtained Pareto-optimal designs. It should be noted that in the present work, the terms individual and design are used interchangeably.

4.2.1. Non-dominated sorting

The parent population P_t and offspring population Q_t are combined to create $R_t = P_t \cup Q_t$ where t denotes the generation number. The combined population R_t is sorted according to non-constrain-domination and the individuals are ranked. Following the definition by Deb [20], an individual $X^{(a)} \in R_t$ is said to constrain-dominate an individual $X^{(b)} \in R_t$, if any of the following conditions are true:

- (1) $X^{(a)}$ and $X^{(b)}$ are feasible, with
 - (a) $X^{(a)}$ is no worse than $X^{(b)}$ in all objectives, and
 - (b) $X^{(a)}$ is strictly better than $X^{(b)}$ in at least one objective.
- (2) $X^{(a)}$ is feasible while individual $X^{(b)}$ is not.
- (3) $X^{(a)}$ and $X^{(b)}$ are both infeasible, but $X^{(a)}$ has a smaller constraint violation.

(29)

Here, the constraint violation $\mathcal{C}(X)$ of an individual X is defined to be equal to the sum of the violated constraint function values [33],

$$\mathcal{C}(X) = \sum_{j=1}^B \mathcal{H}(g_j(X))g_j(X), \quad (30)$$

where \mathcal{H} is the Heaviside step function. The concept of constrain-domination enables us to compare two individuals in

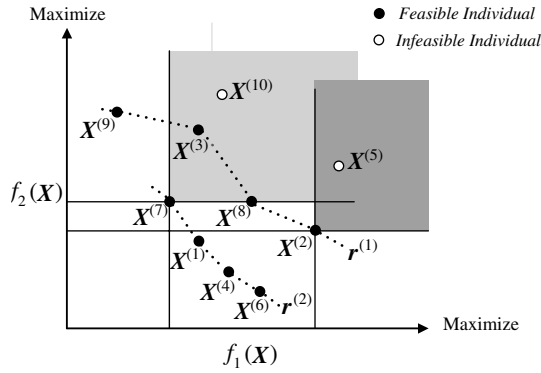


Fig. 3. Depiction of the constrain dominance relations for the simultaneous maximization of two objective functions.

problems that have multiple objectives and constraints, since if $X^{(a)}$ constrain-dominates $X^{(b)}$, then $X^{(a)}$ is better than $X^{(b)}$. If none of the three conditions in (29) are true, then $X^{(a)}$ does not constrain-dominate $X^{(b)}$. Perhaps most easily visualized in the case of two objective functions, Fig. 3 provides a graphical depiction of the dominance relation where two objectives are to be maximized. Shaded regions represent the *line of sight* of a particular individual. When comparing two feasible individuals $X^{(a)}$ and $X^{(b)}$, $X^{(b)}$ is considered to be dominated by $X^{(a)}$ if $X^{(b)}$ is able to see $X^{(a)}$. Conversely, feasible individuals that lack any other feasible individuals in their line of sight are found to be non-dominated. When both solutions are infeasible, the concept is extended to define constrain-domination based on the magnitude of constraint violation. In Fig. 3, $X^{(7)}$ is dominated by $X^{(3)}$ and $X^{(8)}$, since $X^{(3)}$ is strictly better than $X^{(7)}$ in both objectives; and $X^{(8)}$ is equal (no worse) in objective 2, while it is strictly better in objective 1. Although $X^{(5)}$ and $X^{(10)}$, are within the line of sight of $X^{(7)}$, they are infeasible and therefore dominated in all cases by feasible individuals. The non-constrain-dominated set consisting of $X^{(9)}$, $X^{(3)}$, $X^{(8)}$, and $X^{(2)}$, are designated to be of rank 1, denoted by $r^{(1)} = \{X^{(9)}, X^{(3)}, X^{(8)}, X^{(2)}\}$. In order to find the rank 2 individuals, the rank 1 individuals are temporarily discarded from the population and the non-constrain-dominated solutions of the remaining population are found and designated as the rank 2 set. In Fig. 3, $r^{(2)} = \{X^{(7)}, X^{(1)}, X^{(4)}, X^{(6)}\}$. This procedure is continued until the entire population is classified into various subpopulations $r^{(q)}$ of rank q . Infeasible solutions are ranked according to the magnitude of their constraint violation.

4.2.2. Crowding distance

One of the goals of a multi-objective genetic algorithm is to ensure population diversity in the non-dominated set. This is achieved by giving preference to individuals that are more evenly spaced (i.e., less crowded) in the objective space. To this end, the concept of crowding distance is introduced, wherein each individual of a ranked subpopulation is given a crowding distance based on its closeness to adjacent neighbors with equal rank in the objective space.

The crowding distance metric proposed by Deb [20] is utilized, where the crowding distance of an individual is the perimeter of the rectangle with its nearest neighbors at diagonally opposite corners.

4.2.3. Controlled elitism sort

Once individuals of equal rank are sorted in descending order of crowding distance, a controlled elitism mechanism is used to obtain an updated parent population, P_{t+1} , from the combined population R_t . To preserve diversity, the influence of elitism is controlled by choosing the number of individuals from each subpopulation $r^{(q)}$ according to the geometric distribution,

$$S_q = S \frac{1 - c}{1 - c^w} c^{q-1}, \tag{31}$$

to form a parent search population, P_{t+1} , of size S , where $0 < c < 1$. Note that S_q is the number of individuals taken from non-dominated subpopulation $r^{(q)}$ with preference given to those individuals that have a large crowding distance, c is a parameter that governs the shape of the geometric distribution and w is the total number of ranked non-dominated subpopulations that comprise the parent population. This method has been shown to provide improved convergence to the true Pareto-optimal front when compared to a standard elitist NSGA-II [34].

4.2.4. Tournament selection

Now that the parent population, P_{t+1} , has been defined, the next step in the process is the crowded tournament selection routine, where each individual competes in exactly two tournaments with randomly selected individuals, a procedure which imitates survival of the fittest in nature. Individual $X^{(a)}$ is said to win a tournament with individual $X^{(b)}$ if any of the following conditions are true:

- (1) $X^{(a)}$ has a smaller(i.e., better) rank than $X^{(b)}$,
- (2) $X^{(a)}$ and $X^{(b)}$ have the same rank, but $X^{(a)}$ has a larger crowding distance. (32)

In this manner, an intermediate mating pool is generated from the parent population that has a higher occurrence of better ranked and less crowded individuals. Inclusion of the crowded distance metric enables the genetic algorithm to seek out a well distributed Pareto-optimal front.

4.2.5. Crossover and mutation

Uniform crossover and random uniform mutation are employed to obtain the offspring population, Q_{t+1} . An integer representation such as that shown in (28) may be directly manipulated by these operators. The integer-based uniform crossover operator takes two distinct parent individuals and interchanges each corresponding design variable with a probability, $0 < p_c \leq 0.5$. Following crossover, the mutation operator changes each of the children’s integer coded design variable with a mutation probability, p_m , from its current value to a random integer between 0 and \mathcal{J}_{\max} .

5. Results and discussion

The optimal design of functionally graded cylindrical shells that are subjected to either a surface temperature or surface heat flux are presented in this section. The shell geometry is fixed such that the global midsurface radius $R = 0.1$ m and the corresponding angular span is $\Theta = \pi/2$. The length of the shell's midsurface in the circumferential direction is therefore $S = R\Theta = \pi/20$. The circumferential length to thickness ratio is $S/H = 4$. In addition, a flat plate of length $L = \pi/20$ and $L/H = 4$ is also investigated and the results compared to a curved shell for the same loads, objectives, and constraints. The volume fraction distribution in the thickness direction is defined using 11 equally spaced control points. Accordingly, analyses of the FGM plates and shells are performed by partitioning the shell into $N = 10$ continuously graded layers. The power series solution utilizes 10 series terms per layer in (22) and (24) in order to obtain 4 significant digits of accuracy for the temperature and stresses. The volume fraction value at the control points are incremented from 0 to 1 in steps of 0.05 by choosing $\mathcal{J}_{max} = 20$. The genetic algorithm optimization was performed using a search population size of $M = 150$ individuals, crossover probability of $p_c = 0.25$, gene mutation probability of $p_m = 0.135$ and controlled elitism value $c = 0.5$.

5.1. Model problem I

In the first model problem, an isotropic Zirconia/Titanium shell, having a sinusoidal temperature distribution applied to its top surface, is optimized. The stress-free

reference temperature is taken to be $T_{ref} = 300$ °C. The shell is subjected to a sinusoidal temperature change of magnitude 850 °C above the stress-free reference temperature. That is, the temperature of the shell is prescribed to have a peak value of 1150 °C at the midspan of the shell's top surface. The remaining edges are fixed at reference temperature T_{ref} . The analytical solution is used to obtain the temperature field. The constants are chosen as $\vartheta^- = 1, \xi^- = 0, \chi^- = 0, \vartheta^+ = 1, \xi^+ = 0, \chi^+ = 850$ °C, and $k = 1$ in the boundary conditions (19). The material properties for Zirconia, Titanium alloy (Ti-6Al-4V) at the reference temperature of 300 °C are given in Table 1.

The goal of this model problem is to minimize the peak hoop stress σ_{ss} while also minimizing the mass m (per unit axial length). The inner and outer surfaces are constrained to be composed of entirely Titanium and Zirconia, respectively. A constraint is introduced to ensure that the peak temperature experienced by the Titanium phase is less than 600 °C. The objective functions and constraints are formally stated as follows:

Table 1
Material properties of Zirconia, Titanium, Tungsten, and Copper at 300 °C

	ZrO ₂ [35]	Ti-6Al-4V [35]	W [36]	Cu-Cr-Zr [36]
E (GPa)	100.7	93.67	394.7	115.0
ν	0.333	0.3071	0.2822	0.3267
α ($10^{-6}/$ °C)	6.650	11.49	4.1	17.60
κ (W/m°C)	1.868	10.84	147.2	351.0
ρ (kg/m ³)	5917.7	4378.6	19,229	8790

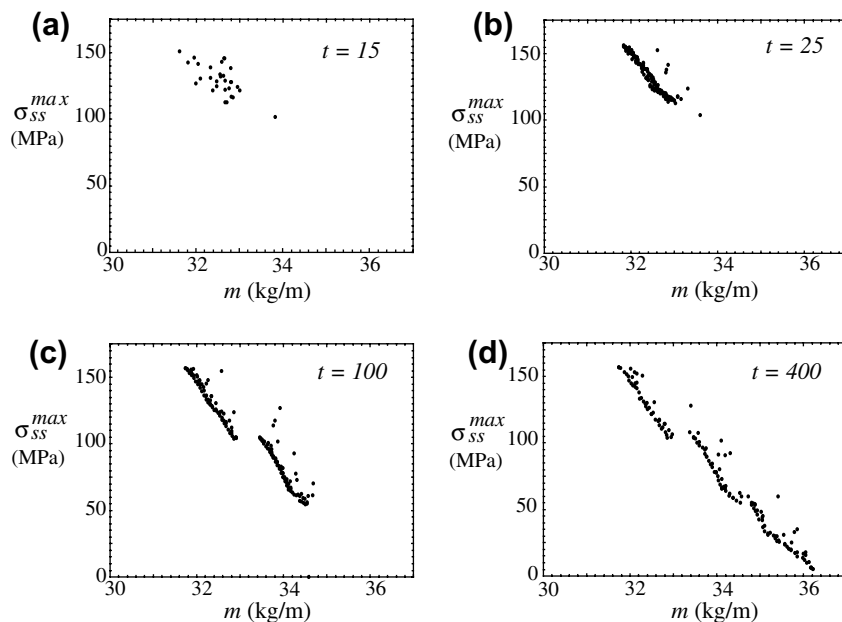


Fig. 4. Plot of the objective function values of individuals in the population at generations $t = 15, 25, 100,$ and 400 for a Zirconia/Titanium cylindrical shell subjected to a temperature load.

Find \mathbf{V} ,

Minimize $f_1(\mathbf{V}) = m = \int_0^\theta \int_{R_i}^{R_o} (V_{ZrO_2} \rho_{ZrO_2} + (1 - V_{ZrO_2})\rho_{Ti})r dr d\theta,$
 $f_2(\mathbf{V}) = \sigma_{ss}^{max} = \max_{x \in D} \sigma_{ss},$ (33)

Subject to $g_1(\mathbf{V}) = T_{Ti}^{max} - 600 \leq 0,$
 $V_1 = 0, V_{N+1} = 1,$
 $0 \leq V_n \leq 1, n = 2, \dots, N,$

where V_n denotes the volume fraction of Zirconia at the control point located at r_n and V_{ZrO_2} is the interpolated value of Zirconia at point in the domain D obtained from (1).

Fig. 4 shows the evolution of the parent population as the algorithm progresses. The objective function values of the parent population, P_t , at $t = 15, 25, 100,$ and 400 generations are depicted in Fig. 4a–d for a curved shell. A total

of 103 Pareto-optimal solutions were identified by the algorithm in 412 generations. In the case of the flat plate, 96 Pareto-optimal solutions were obtained in 434 generations. As it progresses, the algorithm is able to develop new designs with smaller hoop stress. The Pareto-optimal designs for the FGM plate and shell are presented in Fig. 5. It is noted that the Pareto-optimal fronts are discontinuous. For example, the masses of design **B** and **C** are very different, although their maximum hoop stress are nearly the same. Significant reductions in stresses are obtained for moderate increases in mass for both flat plates and curved shells. For example, in the case of the cylindrical shells, design **L** provides a 96.76% reduction in hoop stress for a 14.08% increase in mass as compared to design **G**. It is observed that for a chosen Pareto-optimal design for a graded curved shell, it is possible to find graded flat plate designs that have smaller mass and peak hoop stress.

Fig. 6 shows the through-the-thickness profiles of Zirconia volume fraction for the flat plate designs labelled **A** to **F** in Fig. 5. In this and other figures that follow, H is the total thickness and z is the global thickness coordinate from the midsurface of the plate/shell. The minimum mass design, shown in Fig. 6a, consists of a monolithic region of Zirconia that occupies 30% of the plate’s thickness near the top surface. This acts as a thermal barrier that reduces the maximum temperature experienced by the Titanium to 570.6 °C. The bottom 60% of the plate is composed of a monolithic region of Titanium to reduce the mass and there is a steep grading between the two monolithic regions. Fig. 6 demonstrates that multiple volume fraction profiles give nearly the same thermal barrier protection. For example, designs **B** and **D** both satisfy the temperature constraint within 1 °C, yet design **D** offers a 38.72% reduction

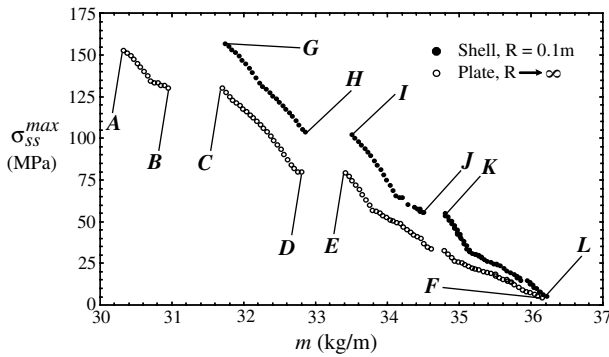


Fig. 5. Pareto-optimal fronts for the Zirconia/Titanium flat plate and cylindrical shell subjected to a temperature load.

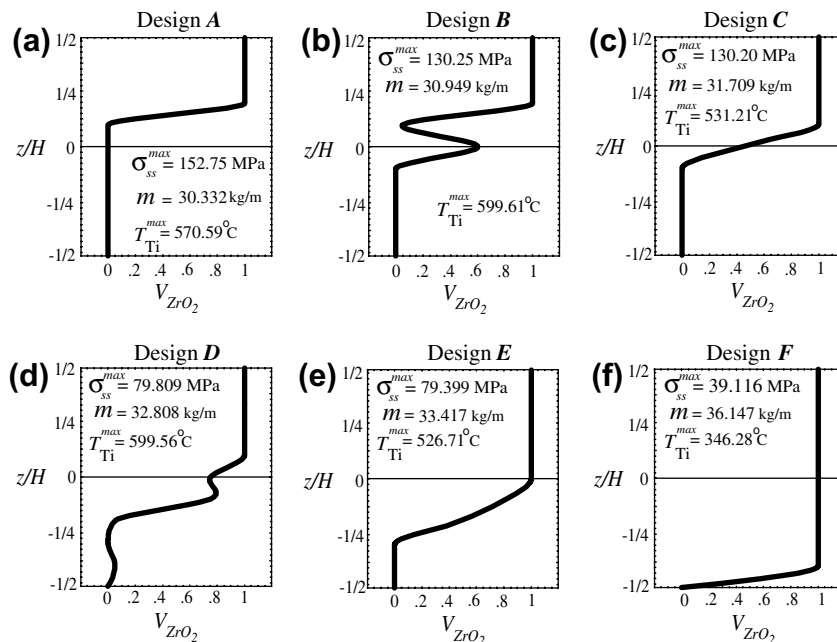


Fig. 6. Volume fraction profiles and performance data for designs **A** through **F** for the Zirconia/Titanium flat plate subjected to a temperature load.

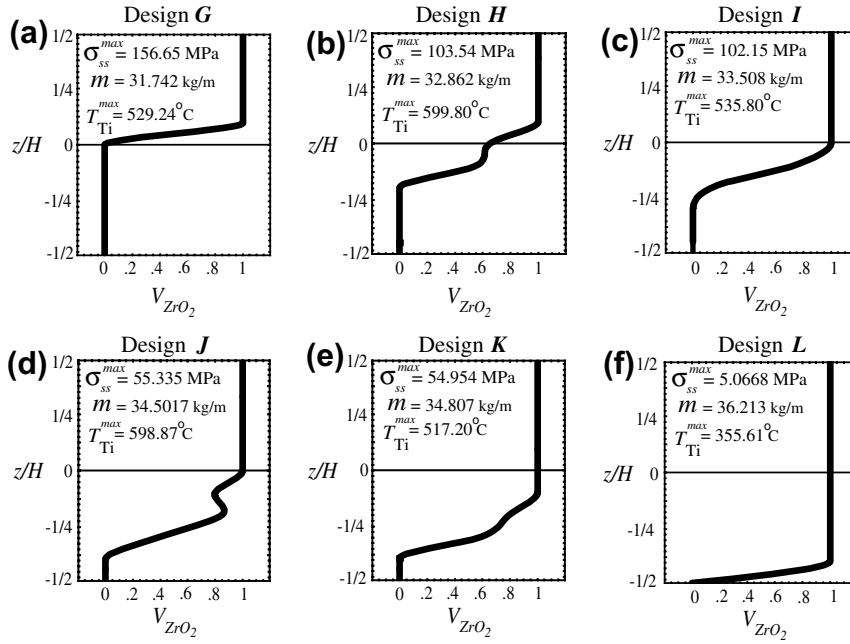


Fig. 7. Volume fraction profiles and performance data for designs G through L for the Zirconia/Titanium cylindrical shell subjected to a temperature load.

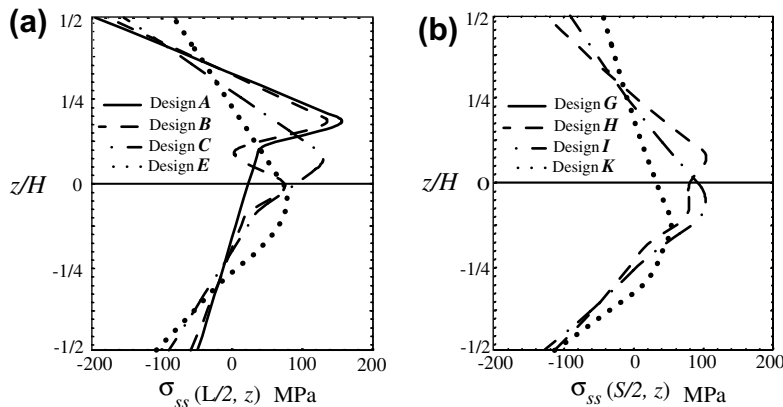


Fig. 8. Through-the-thickness variation of the hoop stress for selected designs of (a) Zirconia/Titanium flat plate and (b) Zirconia/Titanium cylindrical shell subjected to a temperature load.

in peak hoop stress with a 6.0% increase in mass compared to design B.

Through-the-thickness profiles of Zirconia volume fraction for the Pareto-optimal designs G through L for the cylindrical shell are given in Fig. 7. Compared to a flat plate, the minimum mass design for the shell requires at least 40% of its thickness near the top surface to be composed of entirely Zirconia. The volume fraction profile for design L that results in the smallest hoop stress for the cylindrical shell is identical to design F for a flat plate. However, design D for a flat plate is qualitatively different from that of design H for a cylindrical shell, although their mass is nearly identical.

The through-the-thickness variation of the hoop stress corresponding to designs A, B, C, and E for a flat plate are

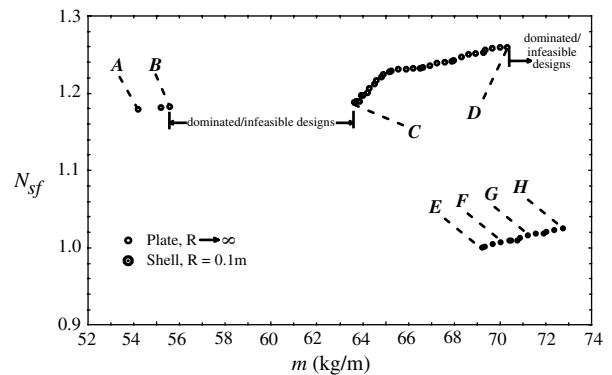


Fig. 9. Pareto-optimal fronts for the Tungsten/Copper flat plate and cylindrical shell subjected to a heat flux load.

shown in Fig. 8a. It shows that the hoop stress σ_{ss} has a continuous variation and the peak tensile value for designs **B** and **C** are essentially the same, although the radial locations where the peak hoop stress values occur are different. The radial variation of the hoop stress corresponding to designs **G** through **L** for a cylindrical shell are depicted in Fig. 8b.

5.2. Model problem II

The second model problem deals with the optimization of isotropic Tungsten/Copper functionally graded plates and shells that are exposed to a sinusoidal heat flux of peak amplitude 1 MW/m^2 on its top surface. The edges and the bottom surface are held at the stress free reference temperature of $300 \text{ }^\circ\text{C}$. The material properties for Tungsten (annealed) and Copper (Cu–Cr–Zr) at the reference temperature of $300 \text{ }^\circ\text{C}$ are given in Table 1. Both Tungsten and Copper exhibit considerable thermal softening and their temperature-dependent yield strengths are as follows [36]:

$$S_y^{(W)} = 679.531 - 1.1877 \tilde{T} + 7.2605 \times 10^{-4} \tilde{T}^2 - 1.4404 \times 10^{-7} \tilde{T}^3 \text{ MPa},$$

$$S_y^{(Cu)} = 299.933 - 0.1286 \tilde{T} - 1.6733 \times 10^{-4} \tilde{T}^2 \text{ MPa},$$

(34)

where $\tilde{T} = T + T_{\text{ref}}$ is the temperature (in $^\circ\text{C}$) at a point.

Since both constituent phases are metallic, the von Mises criterion is used to analyze failure of the W/Cu FGM. The homogenized yield strength of the functionally graded material is based on the following Bishop–Hill upper estimate [37]:

$$S_y = V_W S_y^{(W)} + (1 - V_W) S_y^{(Cu)},$$

(35)

where V_W is the interpolated value of Tungsten at point in the domain D obtained from (1). The objectives of this model problem are to maximize the factor of safety N_{sf} and minimize the mass m , subject to the constraint that the factor of safety be greater than 1.0. The multi-objective optimization problem is stated as follows:

Find \mathbf{V} ,

Minimize $f_1(\mathbf{V}) = m = \int_0^\theta \int_{R_i}^{R_o} (V_W \rho_W + (1 - V_W) \rho_{Cu}) r dr d\theta$, (36)

Maximize $f_2(\mathbf{V}) = N_{\text{sf}} = \min_{x \in D} S_y(\mathbf{x}) / \bar{\sigma}(\mathbf{x})$,

Subject to $g_1(\mathbf{V}) = 1 - N_{\text{sf}} \leq 0$,
 $0 \leq V_n \leq 1, \quad n = 1, 2, \dots, N + 1$,

where V_n is the volume fraction of Tungsten at the control point location r_n and $\bar{\sigma}(\mathbf{x})$ is the von Mises effective stress at a point \mathbf{x} ,

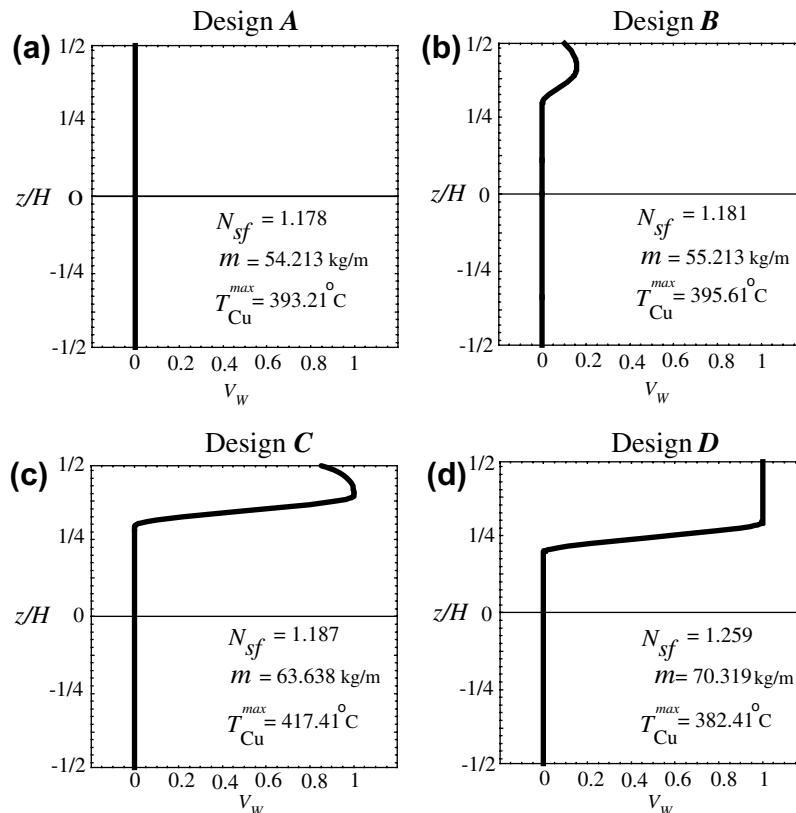


Fig. 10. Volume fraction profiles and performance data for designs **A** through **D** for the Tungsten/Copper flat plate subjected to a heat flux load.

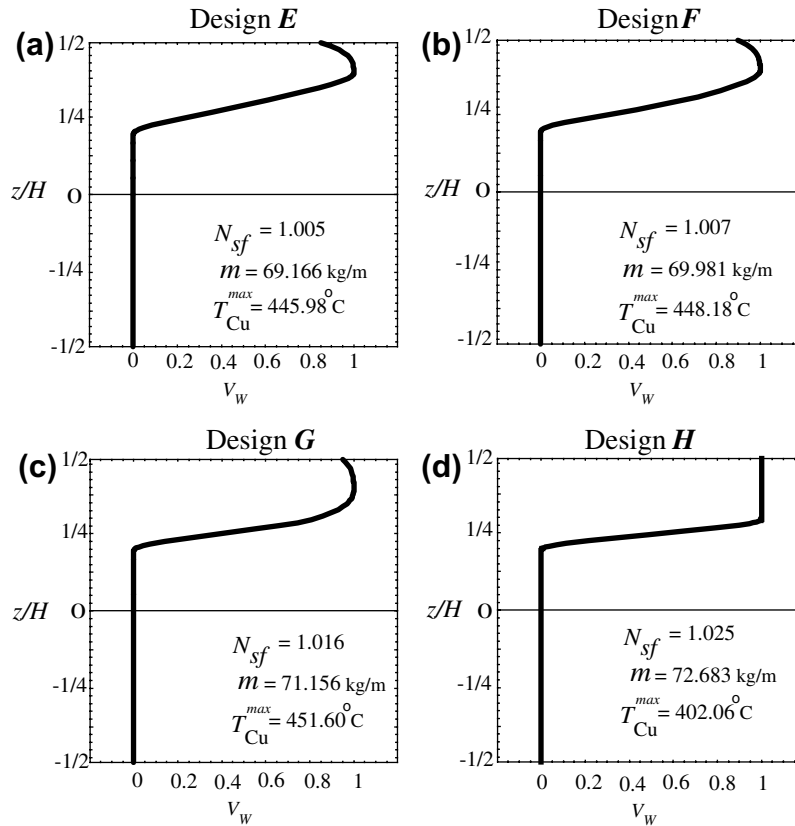


Fig. 11. Volume fraction profiles and performance data for designs *E* through *H* for the Tungsten/Copper cylindrical shell subjected to a heat flux load.

$$\bar{\sigma} = \sqrt{\frac{3}{2} \tilde{\sigma}_{ij} \tilde{\sigma}_{ji}}, \quad \tilde{\sigma} = \sigma - \frac{1}{3} (\text{tr } \sigma) \mathbf{I}. \quad (37)$$

Fig. 9 shows the Pareto-optimal front for W/Cu FGM plates and cylindrical shells obtained using the multi-objective genetic algorithm. It is found that the Pareto-optimal curve is discontinuous between designs *B* and *C*. The factor of safety of *B* and *C* are almost identical although their mass per unit length are 55.213 kg/m and 63.638 kg/m, respectively. Any feasible design with a mass that lies between these two values will have a factor of safety that is smaller than that of design *B* or *C* and thus are dominated/inferior designs. It is found that optimized cylindrical shells have smaller factors of safety than optimized functionally graded plates for the same loading and boundary conditions. This may be attributed to the fact that the shell has a larger surface area on its top surface which is exposed to the heat flux, compared to the flat plate. The volume fraction profiles for the optimized functionally graded plates are shown in Fig. 10. All designs exhibit more than 70% of the shell's thickness to be comprised entirely of Copper. Furthermore, design *A* consists of a monolithic Copper plate that was found to provide a minimum mass per unit shell depth of 54.213 kg/m, but also a minimum safety factor of 1.178. In contrast, design *D* provides a 6.8% increase in strength for a 29.7% increase in mass compared

to design *A*. It is also noted that a monolithic plate of Tungsten is infeasible since it exhibits a safety factor of $N_{sf} = 0.649$. This is due to the fact that the lower thermal conductivity of Tungsten causes the temperature to increase and the yield strength to decrease significantly due to thermal softening. Any design whose mass is greater than that of design *D* is either dominated or it exhibits a factor of safety less than 1.0.

The optimized volume fraction profiles for a cylindrical shell are shown in Fig. 11. Qualitatively, the volume fraction profiles for each shell design is very similar except for subtle variations near the top surface. Furthermore, it is found that unlike a flat plate, a monolithic Copper cylindrical shell is an infeasible design since the factor of safety is less than 1.0.

6. Concluding remarks

A methodology for the multi-objective optimization of functionally graded isotropic plates and shells has been presented. The volume fraction profile is defined using control points that are evenly spaced through the thickness of the shell in conjunction with range-restricted interpolation using Hermite polynomials. The heat conduction and thermoelasticity problems are solved using an exact power series solution to obtain the temperature, heat flux, displacements and stresses. The exact solution

is used to evaluate the objective functions and constraints for candidate designs. The volume fraction values at the control points are chosen as the design variables for the discretely coded elitist multi-objective genetic algorithm.

In the first model problem, functionally graded Zirconia/Titanium plates and shells are subjected to a sinusoidal temperature load on the top surface. They are optimized for minimum hoop stress and minimum mass subject to a constraint on the maximum temperature experienced by the Titanium phase. It is found that significant reductions in hoop stress are obtainable, while only moderately increasing the mass of the plate or shell. It is also found that the optimized flat plate designs dominate the curved shell designs throughout the objective space. In the second model problem, a set of Pareto-optimal designs are obtained for Tungsten/Copper isotropic plate and shells subjected to a sinusoidal heat flux on the top surface, while the remaining surfaces were maintained at the reference temperature. A range of volume fraction profiles are presented for a functionally graded plate with varying degrees of strength and mass, one of which included a pure monolithic Copper plate. The results demonstrate the effectiveness of the proposed methodology for tailoring the volume fraction profile of functionally graded materials used in high temperature and high heat flux applications.

Acknowledgement

The support provided by the U.S. National Science Foundation through Grant DMI-0423485 is gratefully acknowledged.

References

- [1] Miyamoto Y, Kaysser WA, Rabin BH, Kawasaki A, Ford RG. *Functionally Graded Materials: Design, Processing and Applications*. Boston: Kluwer Academic; 1999.
- [2] Federici G, Coad JP, Haasz AA, Janeschitz G, Noda N, Phillipps V, et al. Critical plasma-wall interaction issues for plasma-facing materials and components in near-term fusion devices. *J Nucl Mater* 2000;283–287:110–9.
- [3] Mattas RF, Smith DL, Wu CH, Kuroda T, Shatalov G. Materials issues in the design of the ITER first wall, blanket, and divertor. *J Nucl Mater* 1992;191–194:139–45.
- [4] Vel SS, Batra RC. Exact solution for thermoelastic deformations of functionally graded thick rectangular plates. *AIAA J* 2002;40:1421–33.
- [5] Vel SS, Batra RC. Three-dimensional analysis of transient thermal stresses in functionally graded plates. *Int J Solid Struct* 2003;40:7181–96.
- [6] Ching HK, Yen SC. Transient thermoelastic deformations of 2D functionally graded beams under nonuniformly convective heat supply. *Compos Struct* 2006;73:381–93.
- [7] Ootao Y, Tanigawa Y. Transient thermoelastic problem of functionally graded thick strip due to nonuniform heat supply. *Compos Struct* 2004;63:139–46.
- [8] Zhu H, Sankar BV. Analysis of sandwich TPS panel with functionally graded foam core by Galerkin method. *Compos Struct* 2007;77(3):280–7.
- [9] Tanaka K, Tanaka Y, Enomoto K, Poterasu VF, Sugano Y. Design of thermoelastic materials using direct sensitivity and optimization methods: Reduction of thermal stresses in functionally gradient materials. *Comput Method Appl Mech Eng* 1993;106:271–84.
- [10] Tanaka K, Watanabe H, Sugano Y, Poterasu VF. A multicriterial tailoring of a hollow cylinder in functionally gradient materials: scheme to global reduction of thermoelastic stresses. *Comput Method Appl Mech Eng* 1996;135:369–80.
- [11] Ootao Y, Tanigawa Y, Ishimaru O. Optimization of material composition of functionally graded plate for thermal stress relaxation using a genetic algorithm. *J Therm Stresses* 2000;23:257–71.
- [12] Cho JR, Ha DY. Volume fraction optimization for minimizing thermal stress in Ni–Al₂O₃ functionally graded materials. *Mater Sci Eng A* 2002;334:147–55.
- [13] Cho JR, Ha DY. Optimal tailoring of 2D volume-fraction distributions for heat-resisting functionally graded materials using FDM. *Comput Method Appl Mech Eng* 2002;191:3195–211.
- [14] Lipton R. Design of functionally graded composite structures in the presence of stress constraints. *Int J Solid Struct* 2002;39:2575–2586.
- [15] Turteltaub S. Functionally graded materials for prescribed field evolution. *Comput Method Appl Mech Eng* 2002;191:2283–96.
- [16] Turteltaub S. Optimal control and optimization of functionally graded materials for thermomechanical process. *Int J Solid Struct* 2002;39:3175–97.
- [17] Cho JR, Choi JH. A yield-criteria tailoring of the volume fraction in metal–ceramic functionally graded material. *Eur J Mech A/Solid* 2004;23:271–81.
- [18] Goupee A, Vel SS. Two-dimensional optimization of material composition of functionally graded materials using meshless analyses and a genetic algorithm. *Comput Method Appl Mech Eng* 2006;195:5926–48.
- [19] Pareto V. *Manual of political economy*. New York: A.M. Kelley; 1971.
- [20] Deb K. *Multi-objective optimization using evolutionary algorithms*. Chichester: John Wiley and Sons Ltd.; 2001.
- [21] Huang J, Fadel GM, Blouin VY, Grujicic M. Bi-objective optimization design of functionally gradient materials. *Mater Design* 2002;23:657–66.
- [22] Brodlić K, Mashwama P, Butt S. Visualization of surface data to preserve positivity and other simple constraints. *Comput Graph* 1995;19:585–94.
- [23] Pelletier JL, Vel SS. An exact solution for the steady-state thermoelastic response of functionally graded orthotropic cylindrical shells. *Int J Solid Struct* 2006;3:1131–58.
- [24] Deb K, Agrawal S, Pratap A, Meyarivan T. A fast and elitist multi-objective genetic algorithm: NSGA-II, Technical Report 200001. Indian Institute of Technology, Kanpur: Kanpur Genetic Algorithms Laboratory (KanGAL); 2000.
- [25] Deb K, Agrawal S, Pratap A, Meyarivan T. A fast elitist non-dominated sorting genetic algorithm for multi-objective optimization: NSGA-II. In: *Proceedings of the parallel problem solving from Nature VI (PPSN-VI)*; 2000. p. 849–58.
- [26] Schmidt JW, Hess W. Positivity of cubic polynomial on intervals and positive spline interpolation. *BIT* 1988;28:340–52.
- [27] Lancaster P, Šalkauskas K. Surfaces generated by moving least squares methods. *Math Comput* 1981;37:141–58.
- [28] Hill R. A self-consistent mechanics of composite materials. *J Mech Phys Solid* 1965;13:213–22.
- [29] Hashin Z. Assessment of the self consistent scheme approximation: conductivity of composites. *J Compos Mater* 1968;4:284–300.
- [30] Rosen BW, Hashin Z. Effective thermal expansion coefficients and specific heats of composite materials. *Int J Eng Sci* 1970;8:157–73.
- [31] Nowinski JL. *Theory of thermoelasticity with applications*. Alphen aan den Rijn, the Netherlands: Sijthoff & Noordhoff International Publishers B.V.; 1978.
- [32] Hyer MW, Rousseau CQ. Thermally induced stresses and deformations in angle-ply composite tubes. *J Compos Mater* 1987;21:454–80.

- [33] Deb K. An efficient constraint handling method for genetic algorithms. *Comput Method Appl Mech Eng* 2000;186:311–88.
- [34] Deb K, Goel T. Controlled elitist non-dominated sorting genetic algorithms for better convergence. In: *Proceedings of the first international conference on evolutionary multi-criterion optimization*. Zurich; 2001. p. 385–99.
- [35] Tanigawa Y, Oka N, Akai T, Kawamura R. One-dimensional transient thermal stress problem for nonhomogenous hollow circular cylinder and its optimization of material composition for thermal stress relaxation. *Trans Jpn Soc Mech Eng, Ser A* 1997;40(2):117–27.
- [36] ITER Material Properties Handbook, ITER Document No. S 74 RE 1; 1997.
- [37] Bishop JFW, Hill R. A theory of the plastic distortion of a polycrystalline aggregate under combined stresses. *Philos Mag* 1951;42:414–27.